

Plasma formation during flash sintering of boron carbide – Part I: Plasma characteristics



Christian Bechteler^a, Andrew Gibson^a, Simone Falco^b, Andrew Kirkpatrick^a, Richard I. Todd^{a,*}

^a University of Oxford, Department of Materials, Parks Road, Oxford, OX1 3PH, UK

^b University of Oxford, Department of Engineering Science, Oxford, OX1 3PJ, UK

ARTICLE INFO

Handling Editor: Dr P. Vincenzini

Keywords:

Flash sintering
Plasma
Flashover
Boron carbide
Densification
Silicon carbide

ABSTRACT

In so-called Field Assisted Sintering Techniques such as Spark Plasma Sintering (SPS) or Flash Sintering (FS), ceramic powder compacts are densified at high sample temperature in the presence of an electrical field. The formation of a plasma is often discussed without actual evidence for its appearance. In this work, which is the first of two parts, the mechanisms of plasma formation as well as its properties under FS conditions were investigated. Field induced breakdown of various atmospheres was conducted by a DC-field (up to 350 V/cm) at temperatures between 1000 and 1500 °C. Experiments were conducted both with and without a sample mounted between the electrodes. Alumina, boron carbide and silicon carbide in green or sintered form were used as the samples. The electrical and optical properties of the plasma were characterised, and the early stages were visualised by high-speed camera recordings. The results showed that the breakdown is caused by a flashover mechanism and the conductance of the plasma under the present conditions was of the same order as the conductivity of a boron or silicon carbide green body. Plasma formation did not lead to extensive sintering but the plasma was able to infiltrate the green body and cause transfer of matter from the interior to the surface and beyond. Based on the present results, it seems unlikely that a gas plasma is formed under the normal conditions of SPS or FS.

1. Introduction

In 2010, the first report of flash sintering (FS) by Cologna et al. [1], attracted great attention owing to its rapid densification of ceramics at low environmental temperatures. The fundamental mechanisms involved have been discussed ever since. One accepted mechanism responsible for the fast densification during FS is rapid heating [2–5], which is known to improve the densification of ceramic particle compacts, oxides and non-oxides [6–13] but other mechanisms may also contribute. Since FS combines high electric fields and elevated temperatures, some researchers have proposed that formation of plasmas may also be important [14–17].

It is known that plasmas can be used to achieve rapid heating (10^3 K/min [18]) and densification of metal [18–20] and TiO_2 nanopowders, which were sintered up to 98 % in a DC plasma [18]. 3YSZ has also been densified using Joule heating of the compact by a current supplied using a cold plasma [21]. Although the conditions in these investigations are far from those normally used for FS, it can be concluded that plasmas provide a potential source of heating that can be useful to densify

(ceramic) powder compacts.

In addition, improved microstructures have been demonstrated for carbide and oxide ceramics if a plasma treatment is applied to ceramic powders prior to conventional sintering [22–24]. Such plasma pre-treatments can also change the surface chemistry of alumina powders, leading to more stable water suspensions used for shaping of the green body [25,26], leading in turn to improved final microstructure in the sintered ceramics.

The inclusion of plasmas as a mechanism which improves densification is also often discussed in the context of Spark Plasma Sintering (SPS). However, various experimental investigations have concluded that no plasma is formed under the usual conditions [27–30]. However, plasma has been reported if SPS is conducted at elevated temperatures (>1150 °C) [27] or using conductive powers without the surrounding graphite die at an applied voltage of 50 V (500 V/cm) [28], i.e. in conditions more similar to FS.

Various investigations of FS of oxide ceramics have suggested that atmospheric breakdown followed by plasma or arc formation is possible, even at room temperature. Plasma formation during FS occurs if the

* Corresponding author.

E-mail address: richard.todd@materials.ox.ac.uk (R.I. Todd).

applied electrical field is sufficiently high, usually in the range of several kV/cm, especially if the atmosphere contains water vapour or the sample has absorbed moisture, or at decreased atmospheric pressure [14–17, 21, 29–31]. In some of these investigations a “gas-discharge induced FS” process was investigated [29–32], which enabled heating of the powder compact by the surrounding plasma until the conductivity of the sample exceeded the conductivity of the plasma, leading to a transition towards conventional FS in which Joule heating by passage of current through the sample dominates. Furthermore, it is suggested that the plasma formation is based on surface flashover which happens within a few microseconds.

Although these previous studies demonstrate that a plasma or arc can heat the material by several hundred degrees, the mechanisms involved have not been explored in detail. Also, potential influences of the surrounding plasma on the material and its sintering other than heating, and whether the plasma can enter the powder compact have not yet been studied. Furthermore, only oxide ceramics have been investigated which opens the question about potential plasma formation and its effects during FS of non-oxide ceramics. The potential formation of plasmas at the lower voltages normally applied in FS also remains unexplored.

In this work, the mechanisms involved in the atmospheric breakdown and the subsequent plasma formation as well as the properties of the plasma and its influence on the sintering of the non-oxides SiC and B₄C are investigated. This publication is the first of two articles and is focused on the mechanisms involved in plasma formation and its interaction with green bodies of these non-oxides and, for comparison, Al₂O₃. Part II [33] examines the effect of the plasma on the sintering of non-oxide ceramics.

2. Materials and methods

2.1. Sample preparation

Boron carbide (B₄C) powder (HD20, D₅₀ = 0.3–0.6 µm, Höganäs) was used in the majority of this investigation. 1 wt% PVB was used as binder in ethanol as a solvent to reduce oxidation during processing [34]. Ready-to-sinter silicon carbide (SiC, Starceram SQ, Höganäs) and alumina (Al₂O₃, TM-DAR, Taimei Chemicals) powders were also used in the investigation of plasma formation.

To achieve a homogeneous dispersion of the B₄C, the solvent was heated up to 60 °C under constant magnetic stirring and the binder was slowly added to the heated solvent and homogenised for at least 15 min while stirring. Carbon black (CB) (Monarch 700, Cabot) was added 15 min before the B₄C-powder was added into the solvent and the stirring was maintained for another 30 min. This was for carbothermal reduction of the oxide layer on the carbide particles.

The slurries were ultrasonicated 5 times for 1 min and subsequently ball milled for 24 h. The slurries were then dried in a rotary evaporator for at least 2 h before sieving the dried mass at 150 µm. For some samples zirconia milling balls were used, to dope the B₄C-powder with zirconia. The zirconia wear debris from the milling balls acted as a marker material, easily distinguishable from B₄C in the SEM, to assess transport of material by the action of the plasma. For all other samples B₄C-milling balls were used.

For the investigated Al₂O₃ samples the same procedure, excluding the addition of CB and ball milling, was applied. The ready-to-sinter silicon carbide was used as-received.

The powders were uniaxially pressed (100 MPa) into bar-shaped samples (30 × 5 × 3 mm³) and cold isostatically pressed at 200 MPa. Holes for connecting the tungsten wire electrodes were manually drilled in both ends of the sample using a 1.5 mm drill and carbon paste was applied over both ends including the holes of the sample to reduce contact resistance. For some experiments carbon foil (C-foil) was loosely wrapped around the sample for thermal insulation, which will be investigated in greater detail in Part II of the investigation [33]. A

schematic diagram of the samples used is shown in Fig. 1 a).

2.2. Thermal treatments

Debinding of the non-oxides was conducted in argon (Ar) at 600 °C for 2 h with a heating rate of 300 K/h.

Al₂O₃ samples were debindered in air under otherwise similar conditions and some of the samples were conventionally sintered in air at 1500 °C for 2 h to achieve almost fully dense samples.

FS was executed in a horizontal alumina tube furnace with a tube of length 120 cm, which was calibrated with an external thermocouple prior to the experiments.

The overall furnace setup, including electrodes and sample, is depicted in Fig. 1. A smaller alumina tube, that could be inserted into or withdrawn from the main furnace tube, was used to hold the metal electrodes in place, which were bent around another alumina insert. This setup enabled an appropriate positioning of the sample in the centre of the main tube where the hot region of the furnace is.

An additional piece of graphite foil was placed near the gas inlet to reduce the oxygen partial pressure in the atmosphere.

LabVIEW software was used to control the DC-power supply (EA-PSI 9750-60; EA Elektro-Automatik GmbH Co. KG, Germany) and to record the electrical data.

FS was conducted by heating the furnace up to 1500 °C and initially applying a potential difference of 50 V at constant furnace temperature. For some experiments higher potential differences up to 700 V were applied at furnace temperatures between 1000 and 1500 °C. Dependent on the experiment, the power supply switched to constant power when the defined power level was reached. For all samples shown in this work, the cathode (−) is on the right and the anode (+) on the left side of the sample.

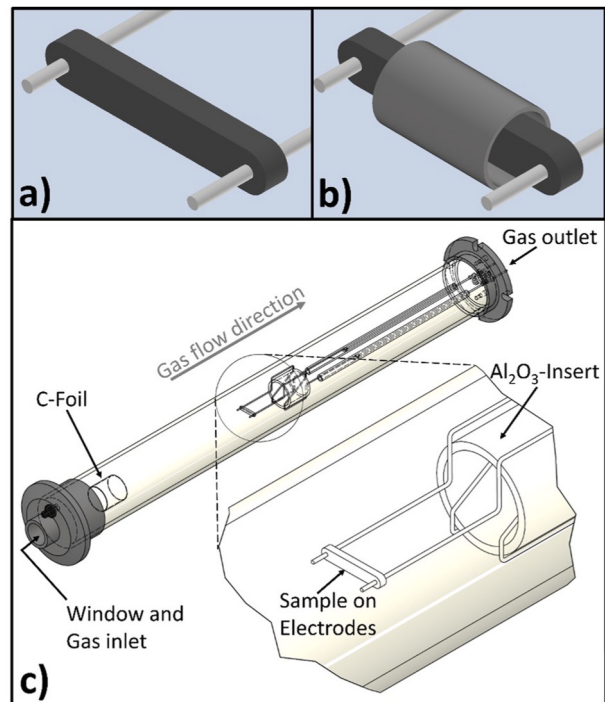


Fig. 1. Schematic diagram of a sample mounted on tungsten (W) electrodes, a) without and b) with C-foil loosely wrapped around the sample for thermal insulation. Cathode (−) is on the right and the anode (+) on the left side of the sample; c) flash sinter setup including horizontal tube furnace, bent electrodes, alumina insert, gas in- and outlet, window and (if applicable) graphite-foil.

2.3. Characterisation

Optical Spectroscopy was conducted using an OceanOptics HDX spectrometer, range 200–1120 nm) as reported in detail previously [4, 35]. Video recordings were made of the experiments (Sony standard video camera) and a high-speed camera (Phantom) with a frame rate of 30,000 fps was used to image the early stages of plasma initiation. All recordings were conducted through the window which was installed on one end of the furnace (Fig. 1c).

FEG-SEM of sintered samples was performed at accelerating voltages between 1 and 10 kV (Zeiss Merlin, Germany). The bulk samples investigated were prepared by sectioning, grinding, and polishing, and mounting on aluminium stubs. EDS was performed using a Bruker FlatQuad windowless EDS detector.

3. Results

3.1. Plasma Pre-Treatment Flash Sintering boron carbide at constant power in Ar

Fig. 2 a) and c) show the electrical parameters measured during FS of B₄C in He under an applied voltage of 50 V (≈ 25 V/cm). The voltage-controlled stage lasted for ~ 3 s before the increase in current led to the transition to power control (700 W, ≈ 2.3 W/mm³).

Video stills of the sample at the different stages of FS can be seen in Fig. 2 i)a – iii)a with the corresponding times shown along the top of the voltage-time plot in Fig. 2 a). During the transition from voltage to power control the current initially concentrated in the sample centre (Fig. 2 ii)a) but heating became more homogeneous during sintering as densification continued (Fig. 2 iii)a). This behaviour resembles that of

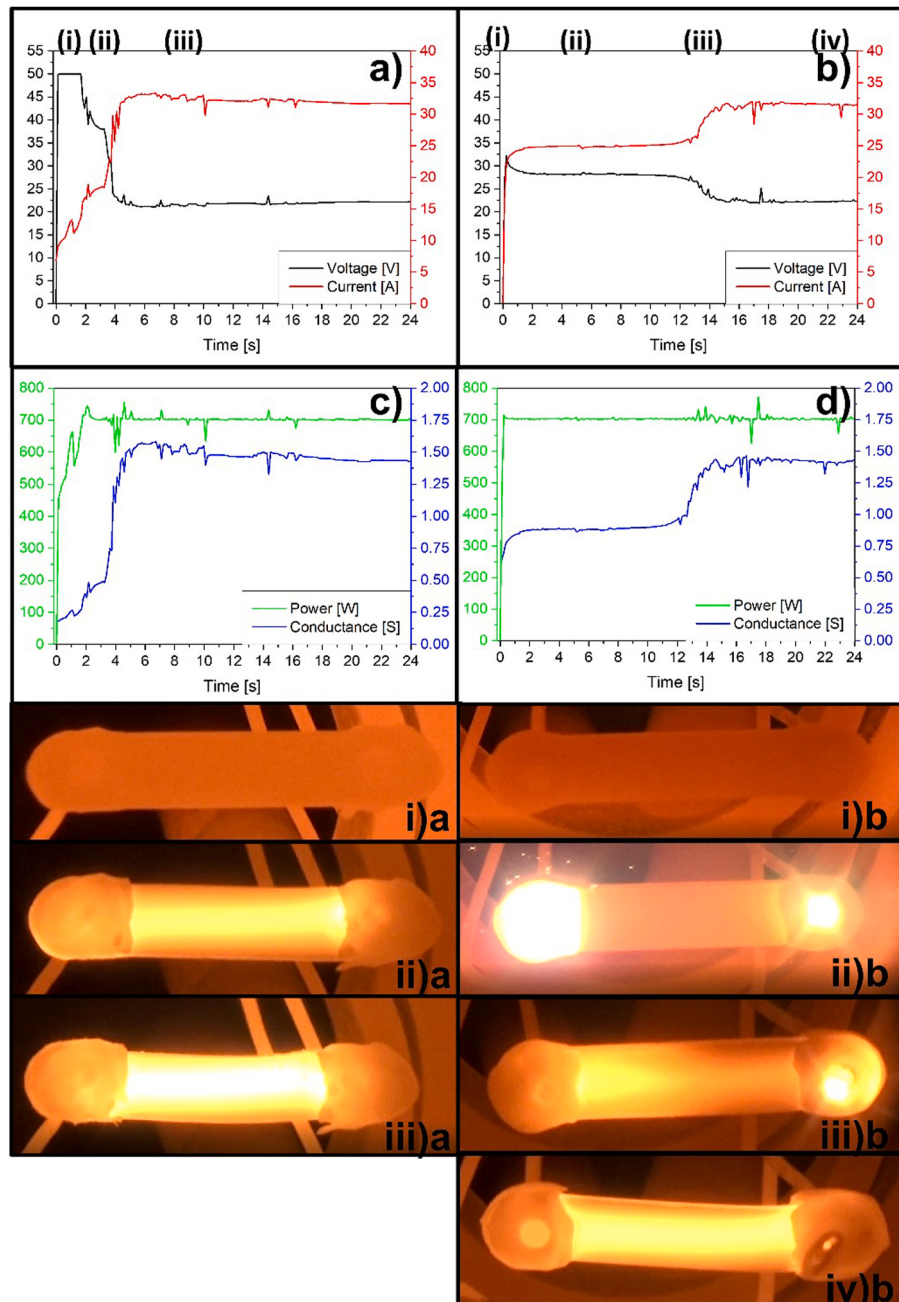


Fig. 2. Electrical parameters (a–d) and sample appearance during FS of B₄C in helium (a and c) and in argon (b and d) which includes the pre-sintering plasma stage. The cathode (–) is on the right and the anode (+) on the left side of the sample.

SiC under similar conditions [36].

The results of using the same electrical parameters and furnace temperature but with an Ar atmosphere are shown in Fig. 2 b) and d). Unlike the previous experiment in He, the switch from voltage to power control occurred after fractions of a second because atmospheric breakdown led almost immediately to plasma formation, which dissipated power at the pre-set limit of 700 W (Fig. 2 ii)b). The plasma remained stable until after ~15 s it collapsed and current flow transitioned into the sample itself (Fig. 2 iii)b), accompanied by another increase in conductance (Fig. 2d). Because of the appearance of the plasma before the transition to FS, this process is described as Plasma Pre-Treatment Flash Sintering (PPT-FS).

The early stages of plasma formation were recorded with a high-speed video camera (Fig. 3). Some initial heating of the electrodes is visible before formation of the plasma (Fig. 3b). It is evident that the initial formation of the arc is on the far side of the sample, where some of the details cannot be seen. However, the discharge around the cathode and bright plasma formation on the far side of the anode as the arc forms in Fig. 3 (c) and (d) show that the preferential path of the plasma was outside the sample and not within the sample itself. Fig. 3 covers 30 ms of the initial plasma formation. The heating of the cathode was concentrated at the tungsten wire, where electrons were emitted. Once the plasma had stabilised, as seen in Fig. 2 ii)b, the anode was hotter than the cathode.

The video images taken throughout the process (Fig. 2 i–iii)b) show that sample heating was slight and shrinkage was negligible during the plasma stage. However, as soon as the plasma collapsed and the transition to current flow within the sample happened, heating and shrinkage of the sample occurred, as can be seen in the videos in the Supplementary Material.

After the plasma collapsed sample heating in Ar was very similar to the experiment conducted in He. Furthermore, the conductance of the samples in both atmospheres remained comparable after ~20 s.

3.2. Electrical characteristics of PPT-FS for boron carbide and silicon carbide

The development of the different stages of PPT-FS were investigated as a function of the pre-set power level for B₄C and SiC. Electrical data recorded during PPT-FS for SiC are shown in the Supplementary Material, Fig. S1. Fig. 4 shows the conductance (I/V) for each stage of the PPT-FS process in Ar for samples each with a different power limit. The

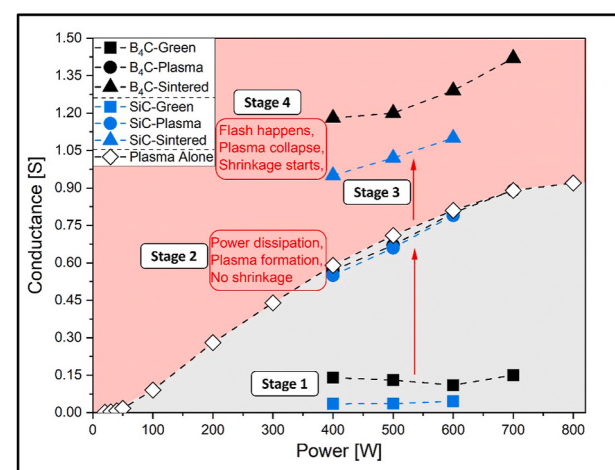


Fig. 4. Conductance (I/V) of B₄C (black) and SiC (blue) as a green body, during the plasma formation and after the plasma collapse and densification of the material towards a sintered material, dependent on the dissipated power. As a reference the white symbols (“plasma alone”) represent the measured conductivity of a plasma for various power dissipations measured in the same setup without a mounted sample. (For interpretation of the references to colour in this figure legend, the reader is referred to the Web version of this article.)

duration of the stage where a plasma was present was typically 15 s for B₄C and 240 s for SiC. For reference the conductance of the plasma itself (“plasma alone” in Fig. 4) was measured in the same setup but without mounting a sample between the W wires (setup shown in Fig. S2 in Supplementary Material).

Stage 1 shows the conductance for green samples measured as a reference value for each sample with a power dissipation of 10 W ($\approx 0.03 \text{ W/mm}^3$) to prevent densification and measure the conductance of the green body. Thus, the power values on the X-axis are not relevant for these data points.

Stage 2 represents the pre-sintering plasma stage where the defined power was dissipated in the plasma, which is why no significant difference in conductance between plasma alone, B₄C and SiC was measurable. Based on this, it can be assumed that the materials’ conductances in this stage were below the conductance of the plasma and the current was mainly flowing through the plasma.

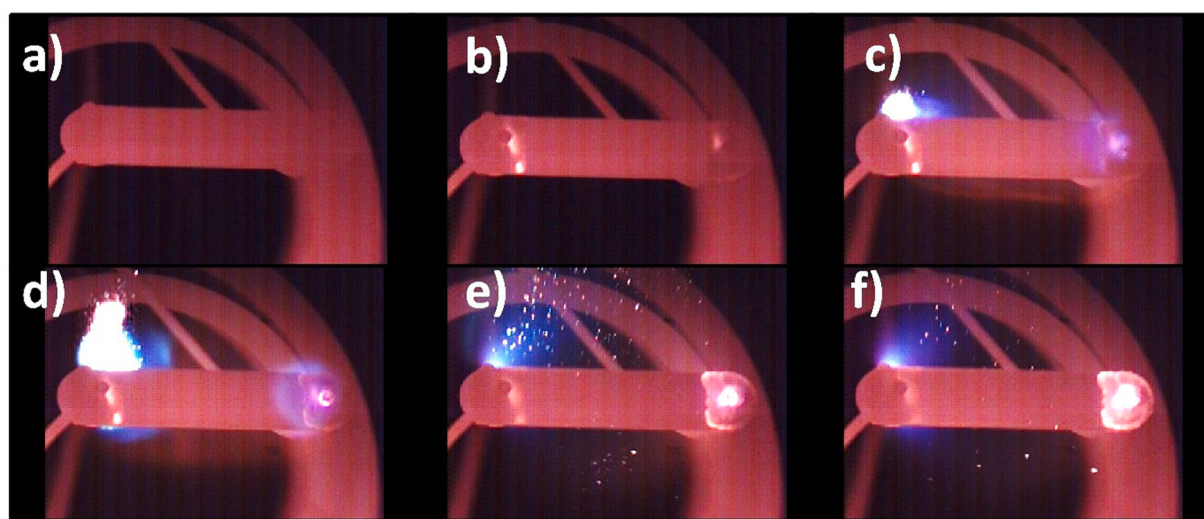


Fig. 3. Images show the high-speed video camera images taken at the very beginning (a) to (f) span 30 ms) of the plasma formation around a B₄C sample (green body) in Ar at 1500 °C furnace temperature. Cathode (–) located on the right, anode (+) on the left side of the sample. (For interpretation of the references to colour in this figure, the reader is referred to the Web version of this article.)

Stage 3 is the transitional stage where the conductance rapidly increased, the plasma collapsed, and the sample began to heat significantly, leading to *Stage 4*.

Stage 4. In this stage a material and power dissipation-dependent conductance can be observed which exceeds the conductance of the plasma alone. This indicates that the solid material became the dominant, high conductance current path, leading to heating of the sample above the furnace temperature.

3.3. Plasma formation under flash sintering conditions

To establish under which circumstances the plasma can form, the breakdown voltage (V_B) was measured under various conditions. Fig. 5 a) shows V_B for the two W wires in the absence of a ceramic sample in various atmospheres (Ar, He, or N₂) and electrode distances of 1 or 2 cm at various temperatures between 1400 and 1500 °C. The closer the electrode distance and the higher the temperature, the lower is V_B . Furthermore, Ar shows the lowest V_B of the three gases, which agrees with the PPT-FS experiments, in which a plasma formed in Ar under the FS conditions used, whereas in He no plasma appeared.

The influence of mounting an electrically insulating or conductive sample on V_B is summarised in Fig. 5 b). Compared to the same experimental setup without a mounted sample, the experiments including a sample showed a substantial decrease in V_B . In the case of an alumina (Al₂O₃) sample, V_B for a green body was lower compared to a fully dense sample. However, no plasma collapse happened with an Al₂O₃ sample even if the plasma was maintained for several minutes because at no point during the experiment did the conductance of the Al₂O₃ exceed the conductance of the plasma.

The Al₂O₃ green body also gave a lower V_B than a B₄C green body over the whole temperature range (1000 °C–1500 °C). At higher temperatures V_B decreased and became similar for all samples.

3.4. Plasma properties under flash sintering conditions

3.4.1. Optical spectroscopy

The plasma properties were characterised to identify its behaviour and potential influence on the material. One way to characterise plasmas and their properties is optical spectroscopy.

Fig. 6 a) shows the spectrum of the emitted light from the Ar-filled alumina tube furnace at 1500 °C without a plasma (0 W) with an Al₂O₃ sample in place. The decay in intensity above 900 nm is an artefact of the spectrometer, the efficiency of which falls to zero at about 1100 nm [4]. It should be noted that these are raw results and have not been corrected for the detector efficiency and other characteristics of the optical setup. The lower wavelength results show the expected black body radiation as well as three sharp peaks at 590, 767 and 770 nm,

which cannot be explained by thermal radiation. Since the peaks were not present if the inside of the furnace tube was covered with C-Foil under otherwise identical circumstances [4,35], these peaks can be associated with light emitted from the alumina tube at this temperature, which is shown in more detail in the Supplementary Material Fig. S4.

When a plasma is formed (>0 W) the overall intensity of the spectra increases with power and additional sharp peaks appear which also increase in intensity with power. The spectrum emitted during the plasma stage with an Al₂O₃ sample in position and a power of 400 W is reproduced in Fig. S5 in the Supplementary Material along with the species responsible for the peaks. With the exception of the peak at 820 nm, all the additional peaks appearing in the presence of the plasma could confidently be assigned to either Al or AlO; none of these peaks was present with a B₄C sample. The peak at 820 nm was present with both B₄C and Al₂O₃ samples and was tentatively attributed to C.

Fig. 6 b) shows the spectrum emitted during the formation of a 400 W Ar plasma around an Al₂O₃ sample compared to the predicted spectrum for a 2250 K black body radiator, calculated using the spectrometer characteristics as described in previous publications regarding optical spectroscopy during FS [4,35]. The general agreement is reasonably good, except for the sharp non-thermal peaks. It is evident from Fig. 2 that most of the visible light emitted whilst the plasma is sustained is from the specimen electrodes so temperatures deduced by this procedure are taken to be an approximation to the electrode temperature.

3.4.2. Plasma conductance

Fig. 6 c) summarises the experimental conductance values for plasmas formed in argon (Ar), helium (He) and nitrogen (N₂) for various power dissipations. A general increase in conductance with power can be seen independent of the atmosphere. However, the conductance in Ar which is ≈ 0.75 S at 500 W is one order of magnitude higher than the conductance in N₂ and about 3 times higher than He if the same power is dissipated. Furthermore, under the present circumstances the conductance for all atmospheres starts to plateau at a certain power dissipation.

If the results from the temperature estimation as in section 3.4.1 and conductance measurements are combined, an almost linear trend for Ar plasma conductance over estimated electrode temperature can be seen (Fig. 6 d). The electrode temperature at the maximum power of 800 W reached ≈2450 K.

3.4.3. Plasma infiltration into powder compacts

Fig. 7 shows a zirconia doped B₄C-sample that was stopped after the pre-sintering plasma stage during PPT-FS, shortly after the plasma collapsed. The SEM image of the polished cross section of the sample in Fig. 7a) shows an elliptical zirconia-depleted region in the centre of the sample. This is visible because of the strong atomic number contrast between the zirconia (light) and the B₄C (dark). The shortest distance

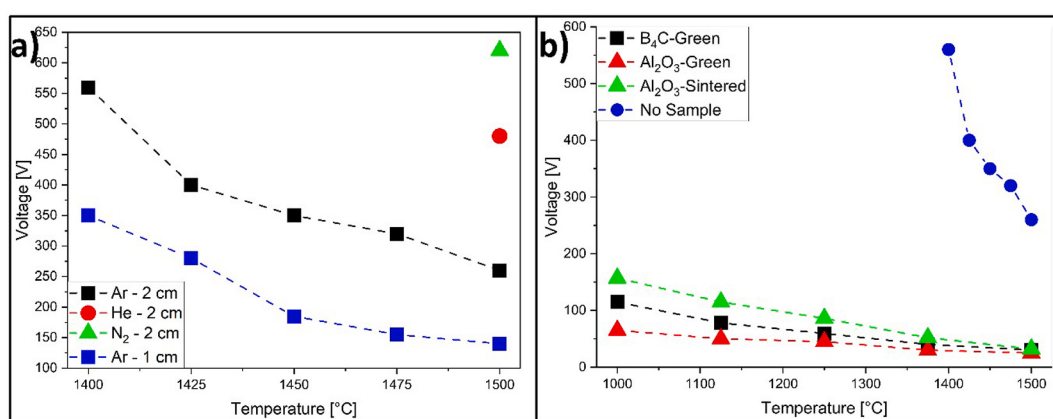


Fig. 5. a) breakdown voltage V_B in different atmospheres and distances without a mounted sample; b) breakdown voltage if samples made from different materials are mounted between the electrodes with a distance of 2 cm.

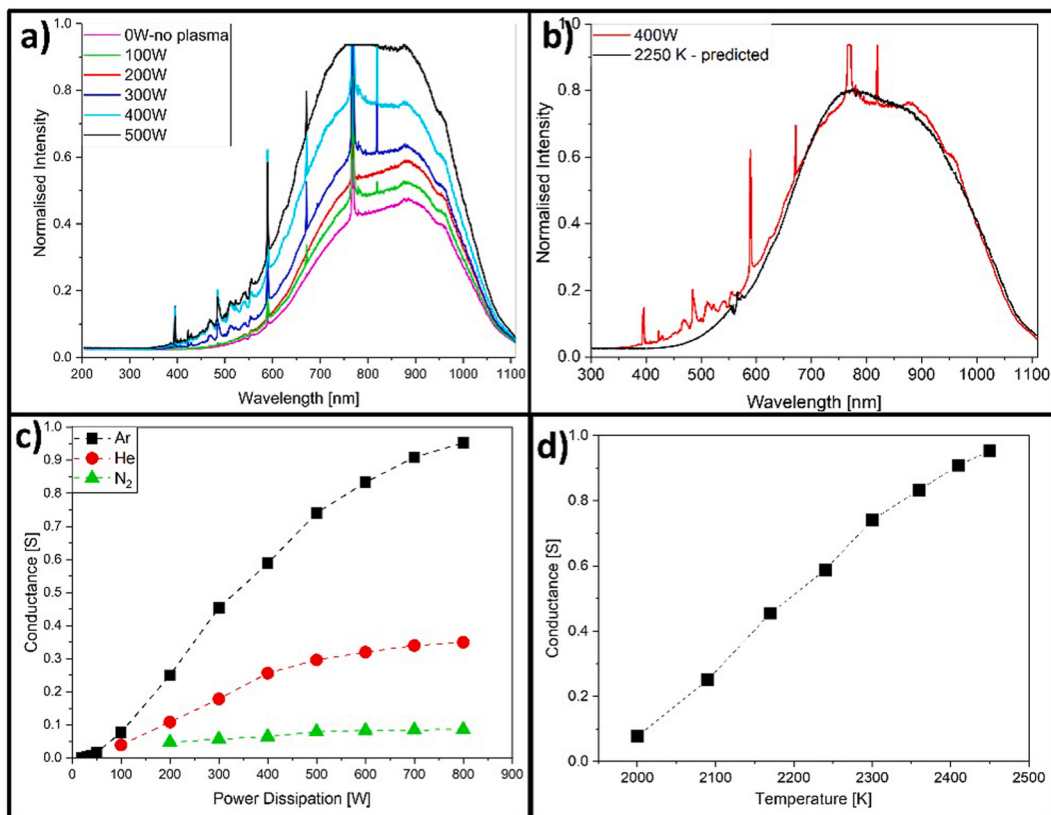


Fig. 6. a) emitted spectra at a furnace temperature of 1500 °C (0 W) in Ar and if a plasma is formed at different power dissipations between 100 and 500 W with an Al₂O₃ sample mounted between electrodes; b) shows the spectrum emitted during the formation of a 400 W plasma in comparison to the predicted spectrum of an ideal black body radiator at 2250 K; c) conductance of plasmas formed in different atmospheres at different power dissipations; d) conductance vs estimated electrode temperature for Ar plasma.

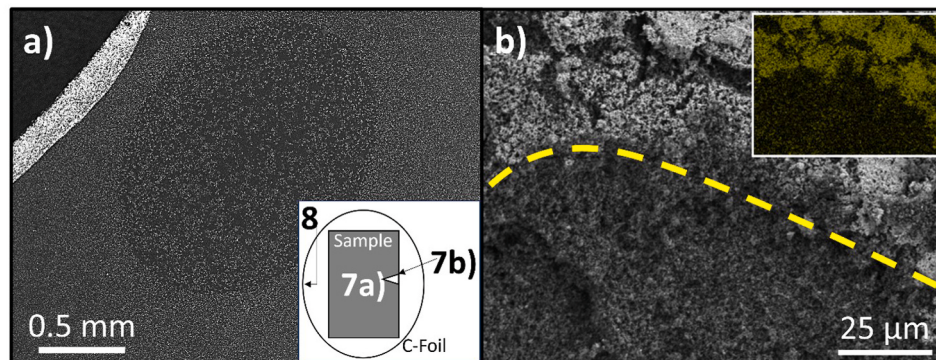


Fig. 7. a) Cross section of a zirconia doped B₄C-sample shortly after the transition from the plasma stage to the Joule heating stage; the insert shows a schematic diagram of the investigated positions of the sample shown in this Figure and Fig. 8, surrounded by a C-Foil loosely wrapped around it; b) surface of the same sample with a scratched region (bottom) and an inserted EDS-map showing the Zr-distribution across the surface.

from the centre of the cross section to the surface of the sample is approximately 1.5 mm.

A layer of redeposited material was found on the surface of this sample. Fig. 7 b) shows a region of the surface that was scratched through to the underlying material. The lower part of the micrograph is the scratch, and the dashed yellow line shows the transition to the surface layer, outside the scratch, in the upper part of the micrograph. The inset shows a Zr EDS map of this image. There is a strong Zr-concentration in the surface layer and a significantly lower Zr-concentration in the material beneath it.

The results of Fig. 7 demonstrate that even before the sintering stage, where Joule heating and densification of the sample are negligible,

transport of material from the interior to the sample to the surface happened during the plasma treatment stage. The zirconia here acted as a marker but it should be noted that carbide was also transported in this way. This is demonstrated by a layer of material that was found to be deposited not only on the sample surface, but also beyond it, on a layer of C-foil that was loosely wrapped around one particular SiC-sample (no ZrO₂ included) for thermal insulation. The redeposited material on both the sample surface and the inside of the foil showed interesting morphologies, some of which are shown in Fig. 8. EDS showed that the redeposited material was mainly Si in this case, indicating that the SiC had decomposed. Furthermore, unusually big, and well-structured crystals were formed found along the cracks on the sample surface

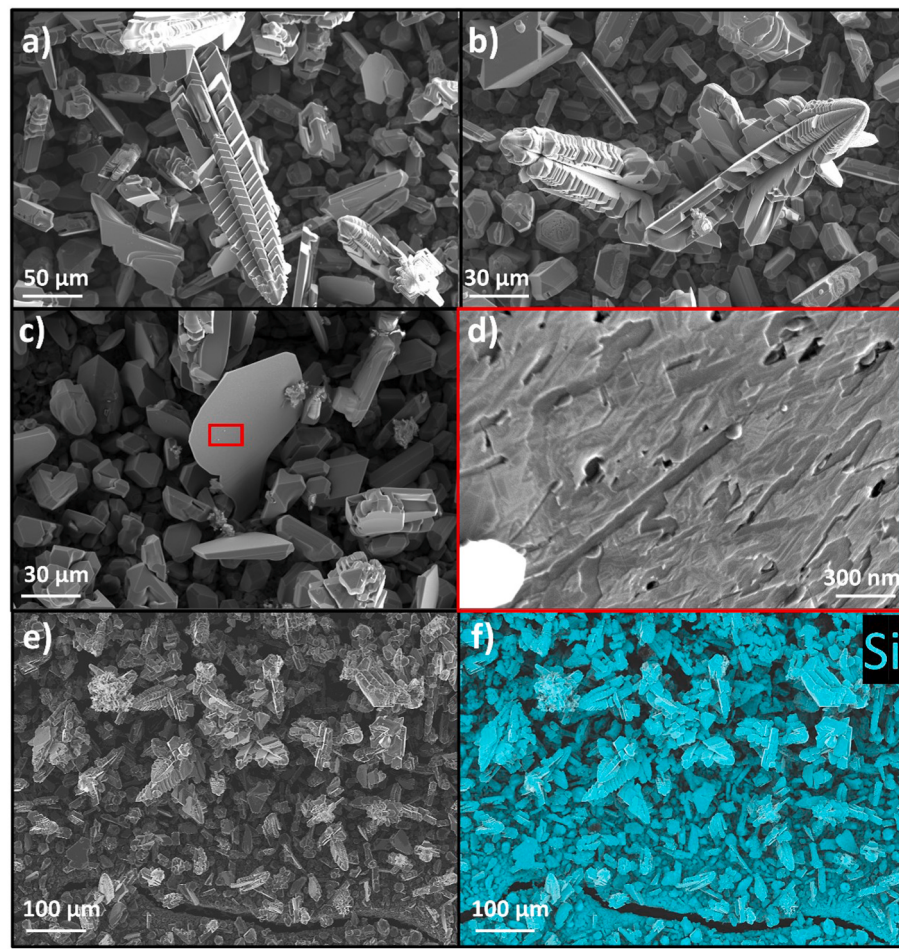


Fig. 8. Structures formed on sample surfaces or C-foil wrapped around a SiC sample during pre-plasma flash sintering as shown in Fig. 1b). d) Is a higher magnification image of the red rectangle in c). e) shows the SEM image of the Si-EDS-map shown in f). (For interpretation of the references to colour in this figure, the reader is referred to the Web version of this article.)

after the plasma stage as is shown in Fig. S6. All these features were absent when a He-atmosphere was used, so that no plasma was formed.

4. Discussion

4.1. Classification of the plasma

The combination of experimental conditions and electrical characteristics indicate that the plasmas generated can be specified as high pressure arc discharge [37]. Compared to other investigations which reported contactless flash sintering based on cold plasmas [21] or plasma electrodes [38], realised by a transformer welder, the conditions of plasma formation and properties are different in this work and the plasma properties can be controlled and adjusted if necessary.

Other investigations of gas discharge induced heating of YSZ from room temperature followed by FS were conducted at various pressures and significantly higher voltages or fields (13 kV [32] or 5.5 kV/cm [31]) which again makes the circumstances of the plasma formation different from this work, but the fundamental mechanisms and properties are similar as will be shown in the following discussion. In Ref. [32] a power dissipation of ≈ 500 W in the generated arc led to a conductance of ≈ 1 mS, which is two orders of magnitude lower compared to the conductance achieved in the N₂ plasma in this work, or three orders of magnitude lower compared to Ar. This can mostly be explained by the temperature difference of ≈ 1500 °C.

4.2. Initial formation of the plasma

As a starting point for understanding the conditions for plasma formation, we first compare the results of the experiments with no sample located between the electrodes with the predictions of Paschen's Law [39–43], in combination with the temperature correction suggested by Peek [42] (see Supplementary Material). Although the trends with electrode separation, temperature and inert gas used are consistent with the predictions of the Paschen equation, the observed breakdown voltages (V_B) are significantly lower than the equation predicts. For example, for an Ar atmosphere under atmospheric pressure (760 Torr) and an electrode distance of 1 cm (without a mounted sample) a V_B of 2.9 kV was calculated for a temperature of 1500 °C, whereas the experimentally obtained value was 150 V for these conditions, Fig. 5a). This is considered to be the result of mechanisms not included in the Paschen approach, which was developed for parallel plate electrodes at low temperature, such as the thermionic emission of electrons from the tungsten wire in the cathode and the field concentrating effect of the wires.

The gases investigated showed different V_B which were lowest for Ar, followed by He and N₂, Fig. 5a). A similar V_B -trend for these gases was suggested in previous investigations [43–45].

When a sample was mounted between the electrodes, the experimental V_B decreased by 80 % at 1500 °C in Ar (Fig. 5 b). This can be explained by a flashover mechanism happening along the solid-gas-interface where a changed electronic structure, due to gas adsorption, solid-gas-reactions, trapping free electrons, or other processes, decreases

breakdown resistance [45–50]. This is an additional mechanism not accounted for in Paschen's law.

The conclusion that flashover is responsible for the initial atmospheric breakdown is supported by previous investigations of gas-discharge induced FS [31,32], conducted at higher voltages (13 kV) and various pressures at room temperature, indicating that as soon as any material is present, flashover is the main mechanism responsible for atmospheric breakdown under a wide range of conditions.

Simulations by Holland et al. [51] have shown that the field strength can be concentrated at small dielectric particles such as those in the green body and indeed the insulating Al_2O_3 as well as the more conductive B_4C green bodies in this work exhibited a lower V_B than sintered Al_2O_3 (Fig. 5b). However, the ability of the dense sintered Al_2O_3 also to induce flashover at a voltage of the same order, and the similarity between the Al_2O_3 and B_4C green bodies, which have very different dielectric constants, suggest that the effects considered by Holland [51] do not have a great influence on plasma formation in this case. It seems likely that the extra surface area for gas absorption etc. in the green body is the main reason that its V_B is lower than for the sintered sample.

4.3. Steady state plasma properties

As is indicated by the higher temperature of the positive electrode in Fig. 2, the electrons in the plasma impart more energy to a surface than the ions, because of the greater mean free path and higher collision frequency of the electrons. The electrons in the plasma are also important to maintaining it, by ionising further Ar atoms. Assuming the size of electrons and the velocity of the ions can be neglected, the mean free path of the electrons, λ , is given by:

$$\lambda = \frac{1}{N\sigma} = \frac{4k_B T}{\pi d^2 P}$$

where N is the number density of atoms, σ is the cross section for electron-atom collisions, k_B is the Boltzmann constant, T is temperature, d is atom/molecule kinetic diameter (He: 260 pm, N₂: 364 pm, O₂: 346 pm, Ar: 340 pm) taken from Refs. [52,53], and P is pressure. For a plasma temperature of ~2000 K, λ is 3 μm in Ar. If the electric field were uniform, this would be much smaller than the distance required for an electron to accelerate to the ionisation energy of an Ar atom (15.7–15.8 eV [53–56]) in between collisions. With the steady state plasma voltage of 27 V in Fig. 2b, the required distance would be > 1 cm. Although electrons can continue to accelerate after a collision that does not remove all of its energy and there is a distribution of path lengths such that many electrons have a greater distance over which to accelerate between collisions, the scale of this disparity suggests that only a small fraction of electrons in the main body of the plasma cause ionisation and that most of the charged particles in the plasma originate from the electrodes and the region of concentrated field in their vicinity. This suggests a rather weakly ionised plasma, as is consistent with the high light emissions from the electrodes compared with the plasma and the lack of Ar emissions in the optical spectrum.

The representative electrode temperature of 2250 K, as estimated from the black body emission fit in Fig. 6b), is similar to the simulated electrode temperatures resulting from the arcs in 3YSZ in air at room temperature in Ref. [32]. The plasma itself emitted less light than the electrodes, because of its rarified nature and the limited extent of ionisation, and its temperature remains unknown. Most importantly for sintering, however, Fig. 2 shows that the specimen temperature is significantly lower than 2250 K during the plasma stage, as is confirmed by the absence of sintering during this stage. This is because most of the electrical power is dissipated at the electrodes and in the plasma outside the sample rather than in the gauge length of the sample.

None of the characteristic peaks associated with Ar plasmas [57,58] was detected in the spectrum in the presence of a plasma, which is consistent with the low emission level from the plasma itself discussed

above. The association of most of the plasma-induced peaks in the presence of an Al_2O_3 sample with Al or AlO demonstrates that these are a consequence of interaction of the plasma with the sample, sputtering material from the surface. The carbon peak at 820 nm was seen with both types of samples and can be attributed to interaction with the carbon paste at the electrodes, where the plasma was most concentrated. No additional peaks were observed with a B_4C sample, possibly because of its refractory nature.

Saunders et al. conducted atomic emission spectroscopy during simulated (F)SPS of W powder in Ar at atmospheric pressure and observed the emission of BBR in combination with many sharp ionisation peaks [28], including some assigned to Ar and W which were absent in the present work despite the use of W electrodes and the same atmosphere. The conditions were more energetic in Ref. [28], however, involving higher currents and powers, which may explain the higher intensity of these characteristic peaks.

4.4. Plasma infiltration of the green body

The results of Figs. 7 and 8 demonstrate unequivocally that the presence of plasma within a green body is possible and that it can interact with the ceramic particles within it. This interaction was not observed without the plasma. The material transported to the surface must therefore have been sputtered from the powders by plasma within the pores of the green body. Although it is evident that the plasma does not lead directly to sintering, it will be shown in Part II of this work [33] that changes to the surface chemistry of the powders have a beneficial effect on sintering during the subsequent stage of flash sintering, in which Joule heating increases the sample temperature (in the absence of a plasma) so that densification occurs. It is therefore important to understand the conditions required for this phenomenon.

The mean free path of ~3 μm is larger than the pores in the green body (powder $d_{50} = 0.3\text{--}0.6$ μm), which suggests that sustaining the plasma independently within the green body would be difficult because only the short electron paths in the distribution would be available for ionisation. Such collisions would be fewer in number and less energetic than those from the longer paths available outside the specimen. We suggest, therefore that the presence of the external plasma may be necessary to supply electrons and ions for the plasma to infiltrate the green body. This is supported by evidence shown in Part II of this work [33] that the effects of the plasma in modifying the surface morphology and chemistry of the carbide powders were significantly more pronounced near the surface of the green body than in the centre of the cross section.

This being the case, it is not entirely clear why the depletion of the zirconia marker material was greatest in the centre of the sample (Fig. 7a). We tentatively attribute this to the temperature gradient within the green body: the hottest part of the system during the plasma stage was evidently the electrodes (Fig. 2b) and heat would have been conducted along the gauge length and lost at the surface, leading to a lower temperature there. The Joule heating of the sample would also contribute to higher temperatures at the centre of the cross section, even though it is relatively small during the plasma stage. Highly refractory ceramic constituents within the plasma would therefore be more liable to condense towards the cooler surface of the sample. The interesting morphologies of the deposits in Fig. 8 are indeed consistent with vapour phase deposition.

The fact that the mean free path is longer than the gaps between adjacent particles in the green body explains why any field-focusing effect of the particles would be ineffective in initiating a plasma in the gas between them (Section 4.2). Thermionic emission from the particles themselves and dielectric breakdown may be possible under some circumstances by field focusing near particle contacts, as has been thoroughly discussed by Holland et al. [51], but no experimental evidence of that was found in this work.

4.5. Collapse of the plasma

The power dissipated within the plasma and electrodes is an important indicator of whether a plasma can be maintained or not. If the power dissipated is high enough, sufficient electrons are being provided by the electrodes and ionisation processes to maintain the plasma as described in the Townsend criterion [40]. This correlation of plasma stability and power dissipated is also demonstrated by the increasing conductance with power shown in Figs. 4 and 6. Conversely, decreasing the power density can lead to the collapse of the plasma. For the “plasma alone” experiments in Fig. 4, for example, the plasma was found to collapse if the power dissipation in the plasma was reduced below 20 W.

In the presence of a ceramic sample, the electrical loading of the plasma and the sample is in parallel and most of the power is dissipated in the component with the higher conductance. Initially, comparison of Fig. 2 a) and ii)a (He atmosphere, no plasma) with 2 b) and 2 ii)b (Ar atmosphere, with plasma), shows that the plasma has a higher conductance than a B_4C green body so that the plasma carries the bulk of the current. As time passes, however, the conductance of the sample increases and, for the sample in Ar, surpasses that of the plasma so that the majority of the power becomes dissipated in the sample and the plasma collapses. This occurs at stage (iii) in Fig. 2b), at a time of ~ 13 s. The increase in conductance of the sample occurs because of (I) the gradual heating from the plasma (both direct and by thermal conduction from the electrodes, Fig. 2 ii)b), (II) the initial stages of sintering, which improves particle-particle contacts [36,59], and possibly (III) because of the cleaning of oxide from the particle surfaces, as suggested by the sputtering effect demonstrated in Figs. 7 and 8, and direct observation in Part II of this work [33]. A similar transition has been shown in other previous work [31,32].

The same competition between plasma and sample explains why no plasma was seen in a He atmosphere under our conditions (Fig. 2a). The He atmosphere was able to withstand the initial voltage applied (50 V) without breaking down so all the current and therefore the electrical power was dissipated in the relatively low conductance green body.

4.6. Relevance to plasma formation in other field assisted sintering techniques

In the general perspective of FS, the results presented confirm that during FS of YSZ or other materials at lower temperature and atmospheres with higher V_B , such as air or N_2 , no plasma formation is involved under the conditions normally used and can be ruled out as a potential sintering mechanism. Also, plasma formation during SPS seems unlikely because usually a carbon die contains the powder and even if the powder is highly insulating, the die itself is sufficiently conductive to conduct the current and prevent the atmosphere from breaking down, which agrees with previously reported results [28].

Nevertheless, a change in atmospheric gas and pressure or the exclusion of a die, as in FSPS, might change the critical conditions for atmospheric breakdown and plasma formation. Furthermore, it should be considered that if a plasma forms it is most likely to happen within fractions of a second at the very beginning when an external field is applied. The rapid increase in conductivity on the initial application of the electric field observed in Fig. 2d) (~ 0.3 s) compared with Fig. 2c) (~ 3 s) is a good indication that a plasma is being formed since it is not controlled by the gradual heating and sintering of the green compact, as is the case in the absence of a plasma.

Another observation that could be an indicator of a plasma is the growth of large and well-structured crystals such as those in Fig. 8 and S6. The growth of crystals aligned with the electric field at surface cracks during FS of ZnO under a high current density was also reported by Zhang et al. [5] and was attributed to a potential liquid phase formation. However, since the hottest part of the sample during FS is the centre, and a crack would interrupt the local current flow, it seems unlikely that the surface region is melted without the interior showing such features.

Plasma formation across the crack, which concentrates the field, provides an alternative explanation for the observed crystal growth.

5. Conclusions

Plasma formation in Ar at a furnace temperature of 1500 °C under FS conditions was investigated. The results suggest that flashover is the fundamental mechanism for atmospheric breakdown, which led to a plasma sustained between the electrodes and around the samples. This was observed with green bodies and pre-sintered specimens of both Al_2O_3 and B_4C .

The plasma formed was classified as high-pressure arc discharge. This did not densify the green bodies but it did lead to transport of matter from within the green body to the surface and beyond by a sputtering effect. Experimental and theoretical arguments suggest that the plasma would be difficult to initiate or sustain independently in the sample interior, but ions and electrons infiltrating the sample from the surrounding plasma may enable limited plasma activity within the sample. It was shown definitively that such a plasma can infiltrate a green body of $\approx 50\%$ density and particle size of 1 μm to a depth of more than 1 mm.

At a certain point the material became more conductive than the plasma, which led to a collapse of the plasma and transition of the current flow into the material itself which, due to Joule heating, then started to densify.

Based on the results, it seems unlikely that such atmospheric plasma formation is involved in normal FS of oxide ceramics or in SPS.

CRediT authorship contribution statement

Christian Bechteler: Conceptualization, Data curation, Formal analysis, Investigation, Methodology, Visualization, Writing – original draft. **Andrew Gibson:** Methodology. **Simone Falco:** Investigation, Methodology. **Andrew Kirkpatrick:** Methodology, Resources. **Richard I. Todd:** Formal analysis, Funding acquisition, Methodology, Project administration, Resources, Supervision, Writing – review & editing.

Declaration of competing interest

The authors declare that they have no known competing financial interests or personal relationships that could have appeared to influence the work reported in this paper.

Acknowledgements

This work was supported by the Engineering and Physical Sciences Research Council [EP/T517811/1] and the Studienstiftung des deutschen Volkes – German Academic Scholarship Foundation.

The authors acknowledge use of characterisation facilities within the David Cockayne Centre for Electron Microscopy, Department of Materials, University of Oxford, alongside financial support provided by the Henry Royce Institute (Grant ref EP/R010145/1).

The authors would like to thank Ocean Insight and Callum Ross for the use of the spectrometer and useful discussions.

Appendix A. Supplementary data

Supplementary data to this article can be found online at <https://doi.org/10.1016/j.ceramint.2024.05.250>.

References

- [1] M. Cologna, B. Rashkova, R. Raj, Flash sintering of nanograin zirconia in 5 s at 850°C, *J. Am. Ceram. Soc.* 93 (11) (2010) 3556–3559, <https://doi.org/10.1111/j.1551-2916.2010.04089.x>.
- [2] R.I. Todd, E. Zapata-Solvas, R.S. Bonilla, T. Sneddon, P.R. Wilshaw, Electrical characteristics of flash sintering: thermal runaway of Joule heating, *J. Eur. Ceram.*

- Soc. 35 (6) (2015) 1865–1877, <https://doi.org/10.1016/j.jeurceramsoc.2014.12.022>.
- [3] I.J. Hewitt, A.A. Lacey, R.I. Todd, A mathematical model for flash sintering, *Math. Model Nat. Phenom.* 10 (6) (2015) 77–89, <https://doi.org/10.1051/mmnp/201510607>.
- [4] C. Bechteler, A. Kirkpatrick, R.I. Todd, Visible light emissions during flash sintering of 3YSZ by thermal radiation, *Scripta Mater.* 219 (2022), <https://doi.org/10.1016/j.scriptamat.2022.114849>.
- [5] Y. Zhang, J.-I. Jung, J. Luo, Thermal runaway, flash sintering and asymmetrical microstructural development of ZnO and ZnO-Bi203 under direct currents, *Acta Mater.* 94 (2015) 87–100, <https://doi.org/10.1016/j.actamat.2015.04.018>.
- [6] W. Ji, B. Parker, S. Falco, J.Y. Zhang, Z.Y. Fu, R.I. Todd, Ultra-fast firing: effect of heating rate on sintering of 3YSZ, with and without an electric field, *J. Eur. Ceram. Soc.* 37 (6) (Jun. 2017) 2547–2551, <https://doi.org/10.1016/J.JEURCERAMSOC.2017.01.033>.
- [7] M. Harmer, E.W. Roberts, R.J. Brook, Rapid sintering of pure and doped alpha-Al2O3, *Trans. J. Br. Ceram. Soc.* 78 (1) (Jan. 1979) 22–25.
- [8] M.P. Harmer, R.J. Brook, Fast firing - microstructural benefits, *Trans. J. Br. Ceram. Soc.* 80 (5) (1981) 147–148.
- [9] I. Wyn Jones, L.J. Miles, Production of beta-Al2O3 electrolyte, *Proc. Br. Ceram. Soc.* (19) (1971) 161–178.
- [10] E.L. Kemer, D.L. Johnson, Microwave plasma sintering of alumina, *Am. Ceram. Soc. Bull.* 64 (8) (Aug. 1985) 1132–1136.
- [11] S. L. Dole and S. Prochazka, "Densification and microstructure development in boron carbide," in Proceedings of the 9th Annual Conference on Composites and Advanced Ceramic Materials: Ceramic Engineering and Science Proceedings, Volume 6, Issue 7/8, vol. 6, W. Smothers, Ed., in Ceramic Engineering and Science Proceedings, vol. 6, Hoboken, NJ, USA: John Wiley & Sons, Inc, 1985, pp. 1151–1160. doi: 10.1002/9780470320280.ch65.
- [12] S.L. Dole, S. Prochazka, R.H. Doremus, Microstructural coarsening during sintering of boron carbide, *J. Am. Ceram. Soc.* 72 (6) (1989) 958–966, <https://doi.org/10.1111/j.1151-2916.1989.tb06252.x>.
- [13] W. Ji, J. Zhang, W. Wang, Z. Fu, R.I. Todd, The microstructural origin of rapid densification in 3YSZ during ultra-fast firing with or without an electric field, *J. Eur. Ceram. Soc.* 40 (15) (Dec. 2020) 5829–5836, <https://doi.org/10.1016/j.jeurceramsoc.2020.07.027>.
- [14] M. Biesuz, P. Luchi, A. Quaranta, V.M. Sgavlo, Theoretical and phenomenological analogies between flash sintering and dielectric breakdown in α -alumina, *J. Appl. Phys.* 120 (14) (Oct. 2016) 145107, <https://doi.org/10.1063/1.4964811>.
- [15] J.-F. Fagnard, et al., Use of partial discharge patterns to assess the quality of sample/electrode contacts in flash sintering, *J. Eur. Ceram. Soc.* 41 (1) (Jan. 2021) 669–683, <https://doi.org/10.1016/j.jeurceramsoc.2020.07.046>.
- [16] R. Chaim, Particle surface softening as universal behaviour during flash sintering of oxide nano-powders, *Materials* 10 (2) (Feb. 2017) 179, <https://doi.org/10.3390/ma10020179>.
- [17] J. Liu, et al., Mechanism of flash sintering with high electric field: in the view of electric discharge and breakdown, *Scripta Mater.* 187 (Oct. 2020) 93–96, <https://doi.org/10.1016/j.scriptamat.2020.06.009>.
- [18] M. Rossetti, G. da S. Falk, A.N. Klein, S.Y. Gómez González, C. Binder, D. Hotza, Plasma-assisted rapid sintering of nanotitanium powders, *J. Eur. Ceram. Soc.* 42 (4) (Apr. 2022) 1670–1684, <https://doi.org/10.1016/j.jeurceramsoc.2021.11.006>.
- [19] H.C. Pavanati, G. Straffolini, A.M. Maliska, A.N. Klein, Microstructural and mechanical characterization of iron samples sintered in DC plasma, *Mater. Sci. Eng., A* 474 (1–2) (Feb. 2008) 15–23, <https://doi.org/10.1016/j.msea.2007.04.020>.
- [20] A.N. Klein, et al., DC plasma technology applied to powder metallurgy: an overview, *Plasma Sci. Technol.* 15 (1) (Jan. 2013) 70–81, <https://doi.org/10.1088/1009-0630/15/1/12>.
- [21] J. Dong, et al., Contactless flash sintering based on cold plasma, *Scripta Mater.* 175 (Jan. 2020) 20–23, <https://doi.org/10.1016/j.scriptamat.2019.08.039>.
- [22] T. Ishigaki, T. Sato, Y. Moriyoshi, M.I. Boulos, Influence of plasma modification of titanium carbide powder on its sintering properties, *J. Mater. Sci. Lett.* 14 (23) (1995) 1694–1697, <https://doi.org/10.1007/BF00422678>.
- [23] D. Lynn Johnson, Microwave and plasma sintering of ceramics, *Ceram. Int.* 17 (5) (Jan. 1991) 295–300, [https://doi.org/10.1016/0272-8842\(91\)90025-U](https://doi.org/10.1016/0272-8842(91)90025-U).
- [24] M.Y. Chen, D.L. Johnson, Effects of additive gases on radio-frequency plasma sintering of alumina, *J. Mater. Sci.* 27 (1) (1992) 191–196, <https://doi.org/10.1007/BF00553855>.
- [25] V. Pouchlý, et al., Improved microstructure of alumina ceramics prepared from DBD plasma activated powders, *J. Eur. Ceram. Soc.* 39 (4) (Apr. 2019) 1297–1303, <https://doi.org/10.1016/j.jeurceramsoc.2018.11.022>.
- [26] Z. Szalay, et al., Atmospheric pressure air plasma treated alumina powder for ceramic sintering, *Ceram. Int.* 40 (8) (Sep. 2014) 12737–12743, <https://doi.org/10.1016/j.ceramint.2014.04.124>.
- [27] R. Marder, C. Estournès, G. Chevallier, R. Chaim, Numerical model for sparking and plasma formation during spark plasma sintering of ceramic compacts, *J. Mater. Sci.* 50 (13) (Jul. 2015) 4636–4645, <https://doi.org/10.1007/s10853-015-9015-z>.
- [28] T. Saunders, S. Grasso, M.J. Reece, Plasma formation during electric discharge (50 V) through conductive powder compacts, *J. Eur. Ceram. Soc.* 35 (3) (Mar. 2015) 871–877, <https://doi.org/10.1016/j.jeurceramsoc.2014.09.022>.
- [29] Y. Li, et al., Flash sintering of high-purity alumina at room temperature, *Journal of Advanced Ceramics* 12 (12) (Dec. 2023) 2382–2388, <https://doi.org/10.26599/JAC.2023.9220816>.
- [30] A. Wu, et al., High-performance ZnO varistor ceramics prepared by arc-induced flash sintering with low energy consumption at room temperature, *High Volt.* 7 (2) (Apr. 2022) 222–232, <https://doi.org/10.1049/hve2.12161>.
- [31] Y. Zhu, et al., Gas-discharge induced flash sintering of YSZ ceramics at room temperature, *Journal of Advanced Ceramics* 11 (4) (Apr. 2022) 603–614, <https://doi.org/10.1007/s40145-021-0561-3>.
- [32] Y. Li, C. Xu, R. Huang, X. Zhao, X. Wang, Z. Jia, Mechanism analysis of arc-induced flash sintering of 3YSZ at room temperature, *J. Eur. Ceram. Soc.* 43 (15) (Dec. 2023) 7033–7040, <https://doi.org/10.1016/j.jeurceramsoc.2023.07.019>.
- [33] C. Bechteler, S. Narayanan, R.I. Todd, Plasma Formation during Flash Sintering of Boron Carbide – Part II: Densification and Material Properties, To be submitted to *Ceramics International*, Mar. 2024.
- [34] C. Xu, Y. Cai, K. Flodström, Z. Li, S. Esmaeilzadeh, G.-J. Zhang, Spark plasma sintering of B4C ceramics: the effects of milling medium and TiB2 addition, *Int. J. Refract. Metals Hard Mater.* 30 (1) (2012) 139–144, <https://doi.org/10.1016/j.ijrmhm.2011.07.016>.
- [35] C. Bechteler, A. Kirkpatrick, R.I. Todd, Comment on 'Flash in argon atmosphere yields electronically conducting yttria-stabilized zirconia at ambient temperature' by Jo et al, *Journal of the American Ceramic Society*, Dec. 2023, *J. Am. Ceram. Soc.* 106 (2023) 5133–5139, <https://doi.org/10.1111/jace.19593>.
- [36] A. Gibson, Y. Li, R.S. Bonilla, R.I. Todd, Pressureless flash sintering of α -SiC: electrical characteristics and densification, *Acta Mater.* 241 (Dec. 2022) 118362, <https://doi.org/10.1016/j.ACTAMAT.2022.118362>.
- [37] S.C. Brown, Introduction to Electrical Discharges in Gases: Electrical Discharges in Gases, Wiley, New York, 1966.
- [38] T. Saunders, S. Grasso, M.J. Reece, Ultrafast-contactless flash sintering using plasma electrodes, *Sci. Rep.* 6 (1) (2016) 27222, <https://doi.org/10.1038/srep27222>.
- [39] G. Galli, et al., Paschen's law in extreme pressure and temperature conditions, *IEEE Trans. Plasma Sci.* 47 (3) (Mar. 2019) 1641–1647, <https://doi.org/10.1109/TPS.2019.2896352>.
- [40] J. Townsend, The theory of ionisation of gases by collision, *Nature* 85 (2152) (Jan. 1911) 400–401, <https://doi.org/10.1038/085400b0>.
- [41] J.R. Roth, Industrial Plasma Engineering: Volume 2 - Applications to Nonthermal Plasma Processing, first ed., CRC Press, London, 2001 [Online]. Available: <https://ebookcentral.proquest.com/lib/gbv/detail.action?docID=5118531>.
- [42] F.W. Peek, Dielectric Phenomena in High-Voltage Engineering, McGraw-Hill Book Company, inc., New York, 1929.
- [43] V.A. Lisovskiy, S.D. Yakovin, V.D. Yegorenkov, Low-pressure gas breakdown in uniform dc electric field, *J. Phys. D Appl. Phys.* 33 (21) (Nov. 2000) 2722–2730, <https://doi.org/10.1088/0022-3727/33/21/310>.
- [44] M.E. Abdel-kader, W.H. Gaber, F.A. Ebrahim, M.A. Abd Al-Halim, Characterization of the electrical breakdown for DC discharge in Ar-He gas mixture, *Vacuum* 169 (Nov. 2019) 108922, <https://doi.org/10.1016/j.vacuum.2019.108922>.
- [45] A. Vlijh, Electric strength and molecular properties of gaseous dielectrics, *IEEE Trans. Electr. Insul.* EI-12 (4) (Aug. 1977) 313–315, <https://doi.org/10.1109/TEL.1977.297984>.
- [46] S. Li, et al., Synergic effect of adsorbed gas and charging on surface flashover, *Sci. Rep.* 9 (1) (Apr. 2019) 5464, <https://doi.org/10.1038/s41598-019-41961-0>.
- [47] E.L. Gurevich, A.W. Liehr, Sh. Amirashvili, H.-G. Purwins, Role of surface charges in dc gas-discharge systems with high-ohmic electrodes, *Phys. Rev. E* 69 (3) (Mar. 2004) 036211, <https://doi.org/10.1103/PhysRevE.69.036211>.
- [48] H.C. Miller, Surface flashover of insulators, *IEEE Trans. Electr. Insul.* 24 (5) (1989) 765–786, <https://doi.org/10.1109/14.42158>.
- [49] H.C. Miller, Flashover of insulators in vacuum: the last twenty years, *IEEE Trans. Dielectr. Electr. Insul.* 22 (6) (Dec. 2015) 3641–3657, <https://doi.org/10.1109/TDEI.2015.004702>.
- [50] M.A. Douar, A. Beroual, X. Souche, Assessment of the resistance to tracking of polymers in clean and salt fogs due to flashover arcs and partial discharges degrading conditions on one insulator model, *IET Gener., Transm. Distrib.* 10 (4) (Mar. 2016) 986–994, <https://doi.org/10.1049/iet-gtd.2015.0751>.
- [51] T.B. Holland, U. Anselmi-Tamburini, D.V. Quach, T.B. Tran, A.K. Mukherjee, Local field strengths during early stage field assisted sintering (FAST) of dielectric materials, *J. Eur. Ceram. Soc.* 32 (14) (Nov. 2012) 3659–3666, <https://doi.org/10.1016/j.jeurceramsoc.2012.03.012>.
- [52] A.F. Ismail, K. Chandra Khulbe, T. Matsuura, Gas Separation Membranes, Springer International Publishing, Cham, 2015, <https://doi.org/10.1007/978-3-319-01095-3>.
- [53] D.W. Breck, Zeolite Molecular Sieves: Structure, Chemistry, and Use, Wiley, New York, 1974.
- [54] R.C. Wetzel, F.A. Baiocchi, T.R. Hayes, R.S. Freund, Absolute cross sections for electron-impact ionization of the rare-gas atoms by the fast-neutral-beam method, *Phys. Rev. A (Coll. Park)* 35 (2) (Jan. 1987) 559–577, <https://doi.org/10.1103/PhysRevA.35.559>.
- [55] B.S. Freiser, Electron impact ionization of argon ions by trapped ion cyclotron resonance spectroscopy, *Int. J. Mass Spectrom. Ion Phys.* 33 (3) (Apr. 1980) 263–267, [https://doi.org/10.1016/0020-7381\(80\)85005-4](https://doi.org/10.1016/0020-7381(80)85005-4).
- [56] K.-M. Weitzel, J. Mähnert, M. Pennro, ZEKE-PEPICO investigations of dissociation energies in ionic reactions, *Chem. Phys. Lett.* 224 (3–4) (Jul. 1994) 371–380, [https://doi.org/10.1016/0009-2614\(94\)00567-2](https://doi.org/10.1016/0009-2614(94)00567-2).
- [57] F. Rezaei, et al., Investigation of plasma-induced chemistry in organic solutions for enhanced electrospun PLA nanofibers, *Plasma Process. Polym.* 15 (6) (Jun. 2018), <https://doi.org/10.1002/ppap.201700226>.
- [58] A. Kramida, Yu.Ralchenko, J. Reader, and NIST ASD Team, "NIST atomic spectra database (version 5.11)," NIST Atomic Spectra Database.
- [59] M. Yoshida, S. Falco, R.I. Todd, Measurement and modelling of electrical resistivity by four-terminal method during flash sintering of 3YSZ, *J. Ceram. Soc. Jpn.* 126 (7) (2018) 579–590, <https://doi.org/10.2109/jcersj2.17256>.